

Structured photoelectron distributions in photodetachment induced by trains of laser pulses: Vortices versus spirals

Lei Geng ¹, F. Cajiao Vélez ^{2,*}, J. Z. Kamiński ², Liang-You Peng ^{1,3,4,†} and K. Krajewska^{2,‡}

¹*State Key Laboratory for Mesoscopic Physics and Frontiers Science Center for Nano-optoelectronics, School of Physics, Peking University, Beijing 100871, China*

²*Institute of Theoretical Physics, Faculty of Physics, University of Warsaw, Pasteura 5, 02-093 Warsaw, Poland*

³*Beijing Academy of Quantum Information Sciences, Beijing 100193, China*

⁴*Collaborative Innovation Center of Extreme Optics, Shanxi University, Taiyuan 030006, China*



(Received 22 July 2021; accepted 30 August 2021; published 16 September 2021)

The formation of quantum vortices in photodetachment by a sequence of left- and right-handed circularly polarized laser pulses in various configurations is analyzed using either the strong-field approximation or numerical solution of the time-dependent Schrödinger equation. Two types of pulse sequences are considered: reducible and irreducible. While the former can be decomposed into series of consecutive and identical (irreducible) subtrains of pulses, the latter cannot be decomposed in that way. As we show, the vortex pattern in the probability amplitude of photodetachment is fully determined by the irreducible pulse configuration. Additional repetitions of an irreducible train create, in the three-dimensional momentum space, nonvortex nodal surfaces, the position of which is estimated. The conditions for the experimental observation of quantum vortices are also determined.

DOI: [10.1103/PhysRevA.104.033111](https://doi.org/10.1103/PhysRevA.104.033111)

I. INTRODUCTION

The first experiments on above-threshold ionization [1] and the low-energy peak suppression in multiphoton electron spectra [2,3] laid the foundations for the rapid development of scientific and technological activities devoted to the study of quantum processes assisted by a strong light field. Further research in this direction culminated in the discovery of high-order harmonic generation [4,5]. The latter has in turn led to the emergence of attophysics [6–8], which deals with phenomena taking place on timescales typical for the electron dynamics in atoms. More or less at the same time, a new method of laser pulse compression was developed [9], allowing not only shortening of its duration to a few femtoseconds, but also significantly increasing the maximum intensity. As a consequence, the area of research on the interaction of strong laser pulses with matter has significantly expanded to include not only nonrelativistic physics [10–18], but also relativistic quantum electrodynamics or plasma and accelerator physics [19–28].

Theoretical studies of multiphoton ionization by strong light fields even preceded the experimental achievements discussed above. We mean here the approach started by Keldysh [29] (see also the recent review articles in [30,31]) and then further developed in various directions by other researchers (see, e.g., [32,33]). This approach is generally called the strong-field approximation (SFA). Moreover, along with the development of computational techniques, the direct numer-

ical solution of the Schrödinger equation is also intensively developed, which allows us to compare the results obtained by this method with the predictions arising from the SFA. However, it should be noted that the approach based on the purely numerical solution of the time-dependent Schrödinger equation (TDSE) also has limitations. The most serious one is its applicability to cases with rather moderate intensities of the laser field. However, if possible, confronting the predictions of the SFA with those obtained by the TDSE analysis is desirable.

The occurrence of the spiral (and presumably also vortex) structures in the photoelectron momentum distributions was predicted theoretically in Refs. [34–36]. The topic was immediately taken up by other theoretical groups (see, e.g., Refs. [37–47]), pointing to the richness of structures that may appear in some particular laser-field configurations as a result of interference of quantum probability amplitudes. However, it is not only a broad theoretical continuation of these investigations that constitutes the essential significance of the approach initiated there, but also their experimental verifications presented afterward in a series of papers [48–52]. These and related explorations create the possibility to investigate (experimentally and theoretically) quantum structures in laser-assisted processes and in general open new directions in strong-field multiphoton phenomena, not only in atomic or molecular physics but also in relativistic quantum electrodynamics, where the pair-creation processes exhibit far-reaching similarities to ionization.

Although the concept of vorticity has existed for a long time [53], its mathematical description in modern physics initially appeared in the works by von Helmholtz [54] and Thomson [55]. In quantum mechanics vortices have been studied by Dirac [56], and the first experimental verification

*felipe.cajiao-velez@fuw.edu.pl

†liangyou.peng@pku.edu.cn

‡katarzyna.krajewska@fuw.edu.pl

of the quantization of velocity circulation was demonstrated in the superfluid He II by Viven [57]. In recent years, we have also seen increased interest in vortices in other types of quantum phenomena [58,59]. In particular, in atomic physics, quantum vortex phenomena have been studied in Refs. [40,41,44,60–66].

Another aspect of this type of investigation is the presence of spiral structures in low-energy photoelectron momentum distributions arising in ionization by two consecutive pulses of opposite circular polarizations [34]. Such momentum distributions have been fully verified experimentally [48,49]. Although spiral structures are commonly associated with the vortex motion, recent studies have shown that these concepts are not necessarily synonymous in quantum mechanics [45]. The point is that vortices in quantum mechanics appear, in the three-dimensional space, as curves (and at the intersections with a plane, mostly as isolated points) where the wave function is zero and its phase is not uniquely defined. This leads to the quantization of the nonvanishing circulation of the wave-function phase gradient, in both position and momentum space [44,67–69]. On the other hand, for spiral structures we deal with surfaces (their intersection with a plane leads to curves similar to the Fermat spirals) where the wave function is reset to zero and its phase, when passing through it, jumps by π . Accordingly, for any closed contour intersecting those nodal surfaces an even number of times, the circulation of the wave-function phase gradient vanishes, provided the contour does not encircle vortex lines. This means that in quantum physics spirals and vortices should be treated as independent concepts. It seems to us that in recent experiments [48,49] only the spiral structures have been detected, whereas the experimental verification of the presence of quantum vortices in ionization by laser pulse configurations proposed in [34] still remains open. In light of these works, we will investigate here the possibility of formation of quantum vortices in photodetachment (or, in general, ionization) and examine how the structured multiphoton peaks are created and controlled by properly adjusted trains of short laser pulses.

The organization of this paper is as follows. In Sec. II we introduce the shapes of the laser pulses considered in our investigations and define their configurations that lead to different spiral and vortex structures. Sections III and IV describe the theoretical tools (i.e., the SFA and TDSE, respectively) used in our studies. Analysis of the vortex and spiral structures for some selected laser train configurations is presented in Secs. V and VI. A summary and conclusions of the possible experimental analysis are presented in Sec. VII.

In our numerical analysis, we use the atomic units of momentum $p_0 = \alpha m_e c$, energy $E_0 = \alpha^2 m_e c^2$, length $a_0 = \hbar/p_0$, time $t_0 = \hbar/E_0$, electric-field strength $\mathcal{E}_0 = \alpha^3 m_e^2 c^3/|e|\hbar$, and laser-field intensity $I_0 = \varepsilon_0 c \mathcal{E}_0^2 \approx 7.02 \times 10^{16} \text{ W/cm}^2$,¹ where m_e and $e = -|e|$ are the electron rest mass and charge,

¹Contrary to very long pulses where the time averaging is applied, we define the atomic unit of intensity as it follows directly from the definition of the Poynting vector. Thus, its value depends only on the electric field and is independent of the polarization properties. In our opinion, for very short pulses, the peak electric field is the most convenient measure of the laser pulse strength.

α is the fine-structure constant, and $\varepsilon_0 = e^2/4\pi\alpha\hbar c$ is the vacuum permittivity. In analytical formulas we set $\hbar = 1$, while keeping explicitly the remaining fundamental constants.

II. LASER PULSE CONFIGURATIONS

In order to define the laser pulse configurations, let us assume that the light field propagates in a direction determined by the unit vector \mathbf{n} . This allows us to introduce two unit and real polarization vectors \mathbf{e}_j ($j = 1, 2$) such that $\mathbf{e}_1 \times \mathbf{e}_2 = \mathbf{n}$. Next we define the vector function

$$\mathbf{F}_\sigma(t) = \begin{cases} \mathcal{N} \sin^2(\frac{\omega t}{2N_{\text{osc}}}) \mathbf{F}_0(t, \sigma) & \text{for } 0 \leq t \leq \tau_p \\ 0 & \text{otherwise,} \end{cases} \quad (1)$$

with

$$\mathbf{F}_0(t, \sigma) = \sin(\omega t + \chi) \mathbf{e}_1 - \sigma \cos(\omega t + \chi) \mathbf{e}_2. \quad (2)$$

Above, the constant \mathcal{N} is chosen such that

$$\max_{t \in [0, \tau_p]} |\mathbf{F}_\sigma(t)| = 1, \quad (3)$$

i.e., the maximum length of the vector $\mathbf{F}_\sigma(t)$ is normalized to 1. Moreover, ω and χ are the carrier frequency and the carrier-envelope phase of the pulse. The duration of a single pulse τ_p is set to $2\pi N_{\text{osc}}/\omega$, where N_{osc} is the number of field cycles. The polarization properties of the field are controlled by σ , and in our further analysis we choose $\sigma = \pm 1$; under this assumption, the normalization factor \mathcal{N} is independent of σ .

Having defined the shape of a single pulse, we can introduce the train of pulses with alternating circular polarizations

$$\mathbf{F}_{\sigma_1 \sigma_2 \dots \sigma_n}(t) = \sum_{\ell=1}^n \mathbf{F}_{\sigma_\ell} \left(t - (\ell - 1)\tau_p - \sum_{\ell'=1}^{\ell-1} D_{\ell'} \right), \quad (4)$$

where $D_{\ell'} \geq 0$ ($\ell' = 2, \dots, n$) represents the time delay of the ℓ th pulse with respect to the preceding one and $D_1 \geq 0$ is the time delay of the first pulse in a train. In the following investigation, we consider such a train of pulses to be in the configuration $(\sigma_1 \sigma_2 \dots \sigma_n)$. For instance, the pulse considered in Ref. [34] was in either the $(+-)$ or the $(-+)$ configuration. In this paper, we will assume that all $D_\ell = 0$. Now we can define the electric field of the pulse

$$\mathcal{E}(t) = \eta_{\mathcal{E}} \mathcal{E}_0 \mathbf{F}_{\sigma_1 \sigma_2 \dots \sigma_n}(t), \quad (5)$$

where \mathcal{E}_0 is the atomic unit of the electric-field strength and the dimensionless parameter $\eta_{\mathcal{E}}$ determines the maximum intensity of the laser pulse. For the case of the non-negative integer $N_{\text{osc}} \geq 2$, the electric field fulfills the condition

$$\int_{-\infty}^{\infty} \mathcal{E}(t) dt = \mathbf{0}, \quad (6)$$

which allows us to introduce the electromagnetic potential in a particular gauge such that

$$\mathbf{A}(t) = - \int_{-\infty}^t \mathcal{E}(t') dt' = \int_t^{\infty} \mathcal{E}(t') dt' \quad (7)$$

and

$$\lim_{t \rightarrow \pm\infty} \mathbf{A}(t) = \mathbf{0}. \quad (8)$$

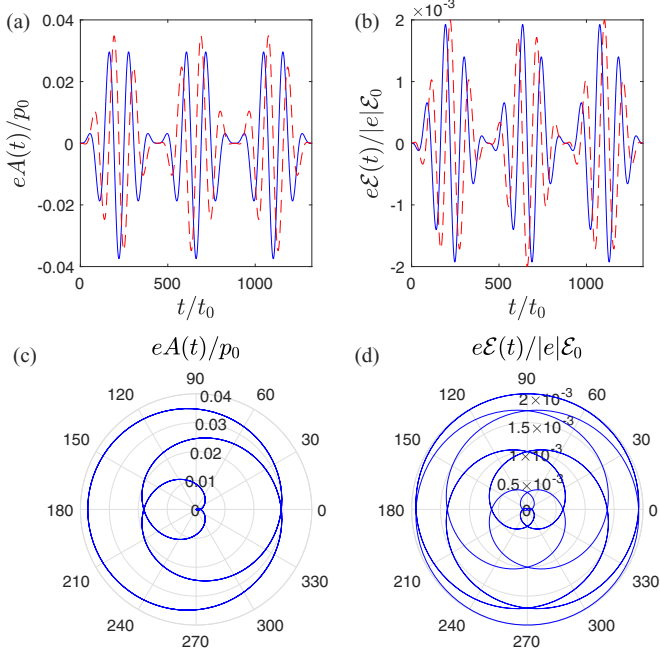


FIG. 1. (a) Vector potential $eA(t)$ and (b) electric field $e\mathcal{E}(t)$, as functions of time, for the driving laser field used in this paper [Eqs. (1)–(7)]. The x components are shown as blue solid lines and the y components are shown as red dashed lines. We consider a train of three laser pulses in the $(+ - +)$ configuration; each one of them comprises four oscillations ($N_{\text{osc}} = 4$). We choose a wavelength $\lambda = 800$ nm ($\omega = 1.55$ eV) and a maximum field strength $\mathcal{E}_{\text{max}} = 0.002\mathcal{E}_0$ ($I_{\text{max}} \approx 2.8 \times 10^{11}$ W/cm 2). Also shown is the time evolution of the tips of the (c) vector potential and (d) electric field in polar coordinates. Both figures start and end at the origin of coordinates and evolve counterclockwise for $\sigma = +1$ and clockwise for $\sigma = -1$. All plots in this figure are presented in atomic units.

In the following discussion, we choose the polarization vectors as $\mathbf{e}_1 = \mathbf{e}_x$ and $\mathbf{e}_2 = \mathbf{e}_y$, the carrier frequency ω corresponds to a wavelength of 800 nm, and the carrier-envelope phase is $\chi = 0$. In Figs. 1(a) and 1(b) we present the x (blue solid lines) and y (red dashed lines) components of the vector potential [Fig. 1(a)] and the electric field [Fig. 1(b)] for a train of laser pulses in the configuration $(+ - +)$ comprising $N_{\text{osc}} = 4$ cycles each. The parameter $\eta_{\mathcal{E}} = 0.002$, which corresponds to the maximum intensity $I_{\text{max}} = 4 \times 10^{-6}\epsilon_0 c \mathcal{E}_0^2 \approx 2.8 \times 10^{11}$ W/cm 2 . In Figs. 1(c) and 1(d) we show the evolution of tips of the vectors $eA(t)$ and $e\mathcal{E}(t)$, respectively, in polar coordinates. Depending on the polarization, the tips rotate either counterclockwise ($\sigma = +1$) or clockwise ($\sigma = -1$).

In Fig. 2 we present the time dependence of the vector potential and the electric field for a train of three pulses in the configuration $(+ + -)$. The remaining field parameters are the same as in Fig. 1. In fact, both plots look quite similar. Nevertheless, due to the interference of probability amplitudes, the photodetachment patterns created by these two configurations are different, as it will be shown shortly.

All configurations of the laser pulse defined by Eq. (5) can be divided into two groups, which we call reducible and irreducible. The reducible configuration $(\sigma_1\sigma_2 \cdots \sigma_n)$ is such

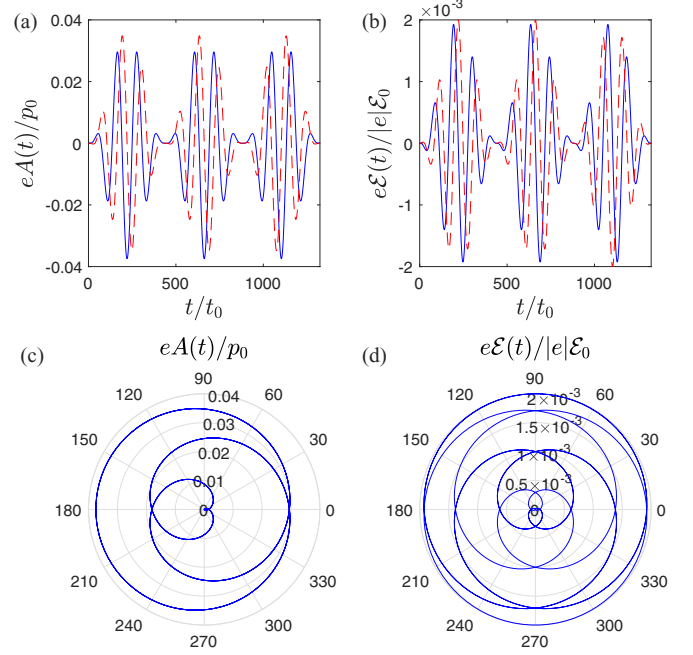


FIG. 2. Same as in Fig. 1 but for the train configuration $(+ + -)$.

that there exist integers k and ℓ for which $n = k \cdot \ell$ and

$$(\sigma_1\sigma_2 \cdots \sigma_n) = [(\sigma_1\sigma_2 \cdots \sigma_k)]^\ell, \quad (9)$$

i.e., the entire train of pulses consists of ℓ identical subtrains. If such a division is not possible then the configuration is called irreducible. For instance, the configurations $(++) = [(+)]^2$ and $(+ - + -) = [(+ -)]^2$ are reducible, but $(+-)$ and $(+ - - +)$ are not. The type of configuration is important as (at least within the SFA with neglected depletion and rescattering processes) the vortex lines are determined only by the irreducible configurations and further repetitions of them do not create new vortex lines but only add extra nodal surfaces.

III. STRONG-FIELD APPROXIMATION

In this section we present the analytical expression for the probability amplitude of photodetachment from negative ions under the scope of the SFA. Even though it has been calculated before (see, e.g., Refs. [66,70]), here we present part of its derivation. Our objective is to determine the transition probability of an electron which in the remote past ($t \rightarrow -\infty$) is found in the bound state $|\Phi_0\rangle$ of the anion and in the far future ($t \rightarrow \infty$) is found in the scattering state of asymptotic momentum \mathbf{p} . (For a discussion about those scattering states, we refer the reader to, e.g., Refs. [65,71,72].) Such a transition is caused by the action of the laser pulse, defined by an oscillating electric field $\mathcal{E}(t)$. Both the single-active-electron approximation and the dipole approximation are used in our derivations. Furthermore, we limit our calculations to the length gauge, as suggested by Gribakin and Kuchiev in Ref. [70].

The theoretical analysis of light-induced photodetachment was, at the beginning, based on complex *ab initio* calculations where electron correlations at the core were assumed to play a major role (see, e.g., [73–75]). However,

Gribakin and Kuchiev [70] demonstrated that it is in fact the proper asymptotic form of the electron wave function which is crucial for a correct treatment of the problem. The authors used a zero-range potential to model the interaction of the outermost electron with the neutral core. Note that the ionization potential of negative ions is considerably smaller compared to their neutral counterparts. This is because the outermost electron is bound by weaker forces than the strong Coulomb force. Hence, the interaction of the laser pulses considered in this paper with an atomic anion will detach the outermost electron with the largest probability. Taking these observations into account, we conclude that the single-active-electron approximation is fully justified in our treatment.

In order to proceed, we first establish the conventions used in this paper. The closure relations for the position and momentum eigenvectors ($|\mathbf{r}\rangle$ and $|\mathbf{k}\rangle$), respectively are

$$\int d^3r |\mathbf{r}\rangle \langle \mathbf{r}| = \hat{1}, \quad \int \frac{d^3k}{(2\pi)^3} |\mathbf{k}\rangle \langle \mathbf{k}| = \hat{1}, \quad (10)$$

where $\hat{1}$ represents the identity operator. The Fourier transform of an arbitrary function $g(\mathbf{r})$ [here denoted by $\tilde{g}(\mathbf{k})$] and the inverse Fourier transform are given by

$$\tilde{g}(\mathbf{k}) = \int d^3r e^{-i\mathbf{k}\cdot\mathbf{r}} g(\mathbf{r}), \quad g(\mathbf{r}) = \int \frac{d^3k}{(2\pi)^3} e^{i\mathbf{k}\cdot\mathbf{r}} \tilde{g}(\mathbf{k}), \quad (11)$$

respectively. This implies that the plane wave is $e^{i\mathbf{k}\cdot\mathbf{r}} = \langle \mathbf{r}|\mathbf{k}\rangle$.

The total energy of the electron can be separated into three parts: a kinetic energy part, represented by the Hamiltonian $\hat{H}_{\text{kin}} = \hat{\mathbf{p}}^2/2m_e$; a potential energy part for the electron-core interaction, represented by $\hat{H}_V = V(\hat{\mathbf{r}})$; and the electron-laser-field interaction part, represented by $\hat{H}_I(t)$. The latter must be specified depending on the gauge being considered. Together, the kinetic and potential energy parts constitute the unperturbed ionic Hamiltonian \hat{H}_{ion} ,

$$\hat{H}_{\text{ion}} = \hat{H}_{\text{kin}} + \hat{H}_V = \frac{\hat{\mathbf{p}}^2}{2m_e} + V(\hat{\mathbf{r}}), \quad (12)$$

while the total Hamiltonian governing the evolution of the electron is

$$\hat{H}(t) = \hat{H}_{\text{ion}} + \hat{H}_I(t). \quad (13)$$

Before the interaction with the laser field starts ($t < 0$) the wave function describing the electron is an eigenstate of \hat{H}_{ion} with eigenvalue E_B , namely,

$$\hat{H}_{\text{ion}}|\Phi_0\rangle = E_B|\Phi_0\rangle, \quad (14)$$

where the stationary eigenstate $|\Phi_0\rangle$ depends on the particular binding potential $V(\hat{\mathbf{r}})$. It has been shown that, for negative ions, zero-range or short-range potentials can be used to model the interaction of the outermost electron with the neutral core [70,76]. We consider a zero-range potential model for our derivations.

According to the description presented above, the probability amplitude of detachment $\mathcal{A}(\mathbf{p})$ is given by

$$\mathcal{A}(\mathbf{p}) = \lim_{t'' \rightarrow \infty} \lim_{t' \rightarrow -\infty} \langle \mathbf{p} - |\hat{U}(t'', t')|\Phi_0\rangle, \quad (15)$$

where $\langle \mathbf{r}|\mathbf{p}-\rangle$ is the scattering state for the ionic Hamiltonian \hat{H}_{ion} with the incoming spherical waves and $\hat{U}(t'', t')$ is the evolution operator associated with the full

Hamiltonian $\hat{H}(t)$ in Eq. (13). This evolution operator contains information about the electron interaction with both the laser field and the binding potential. Its explicit form is in general unknown.

In order to proceed further, we introduce here the Lippmann-Schwinger equation for $\hat{U}(t'', t')$. Namely, we write

$$\hat{U}(t'', t') = \hat{U}_{\text{ion}}(t'', t') - i \int_{t'}^{t''} dt \hat{U}(t'', t) \hat{H}_I(t) \hat{U}_{\text{ion}}(t, t'), \quad (16)$$

where $\hat{U}_{\text{ion}}(t'', t')$ is the evolution operator associated with the ionic Hamiltonian \hat{H}_{ion} presented in Eq. (12). It acts on a bound state $|\Phi(t')\rangle$ as $\hat{U}_{\text{ion}}(t'', t')|\Phi(t')\rangle = |\Phi(t'')\rangle$, i.e., it evolves the wave function from time t' to t'' with $t'' > t'$.

By inserting the Lippmann-Schwinger equation [Eq. (16)] into the expression for the probability amplitude $\mathcal{A}(\mathbf{p})$ [Eq. (15)] we arrive at the formula

$$\begin{aligned} \mathcal{A}(\mathbf{p}) &= -i \lim_{t'' \rightarrow \infty} \int_{-\infty}^{t''} dt \langle \mathbf{p} - |\hat{U}(t'', t) \hat{H}_I(t) |\Phi_0(t)\rangle \\ &= -i \int_{-\infty}^{\infty} dt \langle \Psi_p(t) | \hat{H}_I(t) | \Phi_0(t)\rangle. \end{aligned} \quad (17)$$

Here $|\Phi_0(t)\rangle = e^{-iE_B t} |\Phi_0\rangle$ and in addition we have used the fact that bound and continuum states are orthogonal; in particular, $\langle \mathbf{p} - | \Phi_0\rangle = 0$. We have also introduced the exact scattering state of the electron, defined as $\langle \Psi_p(t) | = \lim_{t'' \rightarrow \infty} \langle \mathbf{p} - | \hat{U}(t'', t)$.

Up to now, the probability amplitude in Eq. (17) has been exact. However, the difficulties in finding an expression for $\hat{U}(t'', t')$ are now transferred into finding the exact scattering state $|\Psi_p(t)\rangle$. The latter also depends on the electron interaction with both the laser field and the binding potential. For this reason, some approximations need to be introduced.

The SFA consists in replacing the exact scattering state by the so-called Volkov solution [77] of a free electron in the laser field [here denoted by $|\psi_p(t)\rangle$]. In other words, it is assumed that the photoelectron does not interact with the residual ion once it is promoted to the continuum. This assumption is fully justified in strong-field photodetachment of negative ions when the binding potential is modeled as a short- (zero-)range potential. In contrast, the predictions arising from the SFA in low-energy photoionization of neutral atoms are expected to depart from experimental observations or *ab initio* calculations. This is due to the long-range nature of the Coulomb potential associated with the positively charged residue.

In the SFA, the probability amplitude of detachments reads

$$\mathcal{A}(\mathbf{p}) = -i \int_{-\infty}^{\infty} dt \langle \psi_p(t) | \hat{H}_I(t) | \Phi_0(t)\rangle, \quad (18)$$

where $|\psi_p(t)\rangle$ and $\hat{H}_I(t)$ are both gauge dependent. By replacing the exact scattering state by the Volkov solution, the gauge invariance of the theory is broken; different results are expected when the velocity or length gauges are used. However, as it was suggested by Gribakin and Kuchiev [70] and later corroborated in Ref. [66], the probability amplitude of detachment is gauge invariant when the binding potential is modeled as a zero-range potential. Moreover, and according to Refs. [44,45], the results obtained from the SFA coincide,

up to a large extent, with the predictions arising from the numerical solution of the TDSE.

We are considering photodetachment driven by finite laser pulses or trains of pulses of *total* duration T_p [for instance, if in Eq. (4) all time delays $D_\ell = 0$, then $T_p = n\tau_p$]. Hence, the interaction Hamiltonian $\hat{H}_I(t)$ vanishes at $t < 0$ and $t > T_p$. In the length gauge, it is given by

$$\hat{H}_I(t) = -e\mathcal{E}(t) \cdot \hat{\mathbf{r}}, \quad (19)$$

while the Volkov solution takes the form

$$|\psi_p(t)\rangle = |\mathbf{\Pi}_p(t)\rangle \exp\left(-\frac{i}{2m_e} \int_0^t dt' \mathbf{\Pi}_p^2(t')\right), \quad (20)$$

where $\mathbf{\Pi}_p(t)$ is the kinetic momentum of the electron in the laser field,

$$\mathbf{\Pi}_p(t) = \mathbf{p} - e\mathbf{A}(t). \quad (21)$$

By inserting Eqs. (19) and (20) into Eq. (18) we find out that the probability amplitude in the length gauge reads

$$\begin{aligned} \mathcal{A}(\mathbf{p}) &= ie \int_0^{T_p} dt \langle \mathbf{\Pi}_p(t) | \mathcal{E}(t) \cdot \hat{\mathbf{r}} | \Phi_0(t) \rangle \\ &\times \exp\left(\frac{i}{2m_e} \int_0^t dt' \mathbf{\Pi}_p^2(t')\right). \end{aligned} \quad (22)$$

From the closure relation for position eigenvectors [see Eq. (10)] we obtain

$$\begin{aligned} \mathcal{A}(\mathbf{p}) &= ie \int_0^{T_p} dt \int d^3r \langle \mathbf{\Pi}_p(t) | \mathbf{r} \rangle [\mathcal{E}(t) \cdot \mathbf{r}] \Phi_0(\mathbf{r}) e^{iG_p(t)} \\ &= ie \int_0^{T_p} dt e^{iG_p(t)} \int d^3r e^{-i\mathbf{\Pi}_p(t) \cdot \mathbf{r}} [\mathcal{E}(t) \cdot \mathbf{r}] \Phi_0(\mathbf{r}). \end{aligned} \quad (23)$$

Here $\Phi_0(\mathbf{r}) = \langle \mathbf{r} | \Phi_0 \rangle$ is the bound-state wave function in position representation and we have introduced the phase

$$G_p(t) = \frac{1}{2m_e} \int_0^t dt' [\mathbf{p} - e\mathbf{A}(t')]^2 - E_B t. \quad (24)$$

Finally, from the definition of the Fourier transform given by Eq. (11) and by noting that $\nabla_k e^{-ik \cdot \mathbf{r}} = -i\mathbf{r} e^{-ik \cdot \mathbf{r}}$ (∇_k is the gradient calculated over the momentum coordinates \mathbf{k}), we arrive at

$$\mathcal{A}(\mathbf{p}) = ie \int_0^{T_p} dt \mathcal{E}(t) \cdot \tilde{\Phi}_0(\mathbf{p} - e\mathbf{A}(t)) e^{iG_p(t)}, \quad (25)$$

where we have introduced the function

$$\tilde{\Phi}_0(\mathbf{k}) = i\nabla_k \tilde{\Phi}_0(\mathbf{k}). \quad (26)$$

The set of equations (24)–(26) is the starting point for our numerical calculations.

We are interested in the photodetachment from the H^- anion in its ground state (s state). As it was done before (see Refs. [44,45,66,70]), we use the zero-range potential to model the electron interaction with the core. Under such circumstances, the bound-state wave function $\Phi_0(\mathbf{r})$ is [70,76]

$$\Phi_0(\mathbf{r}) = \Phi_s(\mathbf{r}) = \frac{A}{\sqrt{4\pi a_0}} \frac{e^{-\kappa r/a_0}}{r}. \quad (27)$$

Here κ and A are dimensionless parameters that depend on the particular anion. While κ is determined by the experimental value of the ionization potential (or electron affinity) as $E_B = -(\alpha m_e c)^2 \kappa^2 / 2m_e$, the parameter A can be obtained by comparison with other *ab initio* calculations. In this paper we use the values suggested by Gribakin and Kuchiev [70], $\kappa = 0.2354$ and $A = 0.75$, such that $|E_B| = 0.754$ eV.

The Fourier transform of the ground-state wave function [Eq. (27)] is [44,45,66,70]

$$\tilde{\Phi}_s(\mathbf{k}) = \frac{2\sqrt{\pi/a_0}A}{(\kappa/a_0)^2 + \mathbf{k}^2} \quad (28)$$

and the function $\tilde{\Phi}_s(\mathbf{k})$ for s states, as defined in Eq. (26), is given by

$$\tilde{\Phi}_s(\mathbf{k}) = -\frac{4i\sqrt{\pi/a_0}A}{[(\kappa/a_0)^2 + \mathbf{k}^2]^2} \mathbf{k}. \quad (29)$$

Finally, with the electric field of the pulse (or series of pulses) given in Eq. (5), we can calculate the probability amplitude of detachment $\mathcal{A}(\mathbf{p})$ under the SFA framework. The time integral in Eq. (25) is performed numerically.

IV. TIME-DEPENDENT NUMERICAL ANALYSIS

In this section we summarize the main aspects of solving the TDSE (for further details, see Refs. [44,45]).

The electron evolution in photodetachment is governed by the full Hamiltonian $\hat{H}(t)$ shown in Eqs. (12) and (13), i.e.,

$$\hat{H}(t) = \frac{\hat{\mathbf{p}}^2}{2m_e} + V(\hat{\mathbf{r}}) + \hat{H}_I(t). \quad (30)$$

For our computational model, we assume that the effective binding potential can be described as a short-range (Yukawa) potential

$$V(\mathbf{r}) = -\beta \frac{e^{-\gamma r}}{r}, \quad (31)$$

where the parameters $\beta = 1.1\alpha c$ and $\gamma = 1/a_0$ guarantee that the bound-state energy E_B corresponds to the measured value for the H^- anion. The numerical method presented here is gauge invariant and, in contrast to the SFA treatment, we consider only the velocity gauge for our calculations. In doing so, we write the interaction Hamiltonian (up to the linear term in the vector potential) as

$$\hat{H}_I(t) = -\frac{e}{m_e} \mathbf{A}(t) \cdot \hat{\mathbf{p}}. \quad (32)$$

Taking into account Eqs. (31) and (32), the full Hamiltonian [Eq. (30)], in position representation, reads

$$\hat{H}(\mathbf{r}, t) = -\frac{1}{2m_e} \nabla^2 + i\frac{e}{m_e} \mathbf{A}(t) \cdot \nabla - \beta \frac{e^{-\gamma r}}{r}. \quad (33)$$

We are interested in finding the solution $\psi(\mathbf{r}, t)$ to the differential equation

$$i\partial_t \psi(\mathbf{r}, t) = \hat{H}(\mathbf{r}, t) \psi(\mathbf{r}, t). \quad (34)$$

To this end, we expand the electron wave function in a (truncated) basis of spherical harmonics. Namely, in spherical

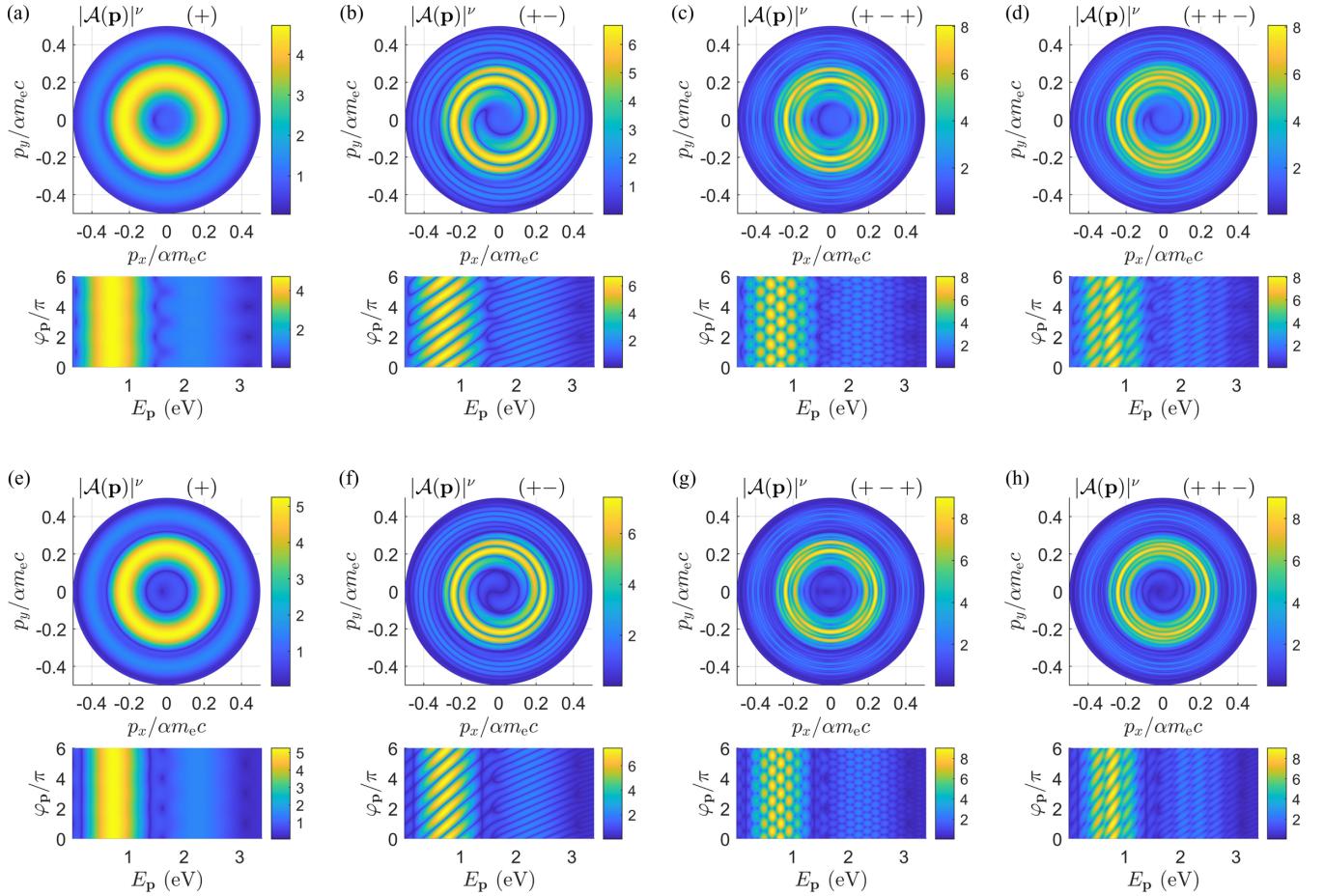


FIG. 3. SFA analysis of photodetachment for four different irreducible configurations of trains of pulses containing (a)–(d) $N_{\text{osc}} = 4$ cycles and (e)–(h) $N_{\text{osc}} = 5$ cycles, for $\theta_p = 0.5\pi$. The remaining laser-field parameters are $\omega = 1.5498$ eV (which corresponds to a wavelength of 800 nm), $\eta_{\mathcal{E}} = 0.002$, and $\chi = 0$ and all the time delays are $D_{\ell} = 0$ [see Eqs. (1)–(4)]. As expected, an increasing number of laser cycles in each individual pulse leads to narrower multiphoton peaks. The amplitudes $\mathcal{A}(\mathbf{p})$ are presented in atomic units and $\nu = 1/2$ is chosen for visual purposes. While the circular plots show the magnitude of the probability amplitude as a function of p_x and p_y , the rectangular plots show the same but as a function of the photoelectron kinetic energy E_p and azimuthal angle φ_p . The latter changes from 0 to 6π , i.e., we show three copies of the distribution from 0 to 2π .

coordinates (r, θ_r, φ_r) ,

$$\psi(\mathbf{r}, t) \approx \sum_{l=0}^{l_{\max}} \sum_{m=-l}^l \frac{\psi_{lm}(r, t)}{r} Y_{lm}(\theta_r, \varphi_r). \quad (35)$$

The functions $\psi_{lm}(r, t)$, which guarantee that Eq. (34) is satisfied, are determined numerically. In doing so, the radial coordinate is discretized according to the finite-difference method. Furthermore, the evolution forward in time is determined by means of the Crank-Nicolson method. Once the coefficients $\psi_{lm}(r, t)$ are found, the probability amplitude of detachment is directly calculated [44,45],

$$\begin{aligned} \mathcal{A}(\mathbf{p}) = & \frac{2\pi}{p} \sum_{l,m} (-i)^l e^{i\delta_l} Y_{lm}(\theta_p, \varphi_p) \\ & \times \int_0^{r_{\max}} dr r \psi_{lm}(r, t_f) R_{pl}(r). \end{aligned} \quad (36)$$

Here r_{\max} is the maximum value for the radial integration and t_f is the final time of propagation; δ_l defines the phase shift and $R_{pl}(r)$ is the radial part of the scattering state of the field-free

effective potential $V(\mathbf{r})$. We have also introduced the spherical coordinates in momentum space (p, θ_p, φ_p) . Equation (36) will be used for our numerical illustrations.

In solving the TDSE we have used $l_{\max} = 5$ [see Eq. (35)]. While the propagation in time is done in steps $\delta_t = 0.05t_0$, the propagation in space is done with $\delta_r = 0.1r_0$. We have chosen the number of radial points to be 1.12×10^5 . Those parameters ensure that convergence is achieved.

V. IRREDUCIBLE CONFIGURATION OF PULSES

In our previous study [45] we analyzed photodetachment driven by laser pulses (or trains of pulses) comprising three cycles within a \sin^2 envelope and with a wavelength of 4000 nm. In order to investigate up to what extent the results presented there are independent of the laser pulse frequency and its time duration, we consider now a light field which is more commonly used in strong-field physics. Namely, we are interested in analyzing photodetachment driven by laser pulses of wavelength 800 nm ($\omega \approx 1.5498$ eV) and comprising $N_{\text{osc}} = 4$ or 5 cycles. In Fig. 3 we present the modulus

of the probability amplitude of detachment $\mathcal{A}(\mathbf{p})$ (raised to the power $\nu = 1/2$, for visual purposes) in the plane defined by the polar angle of electron detection $\theta_p = 0.5\pi$. The number of field oscillations within a single pulse is $N_{\text{osc}} = 4$ [Figs. 3(a)–3(d)] or $N_{\text{osc}} = 5$ [Figs. 3(e)–3(h)]. For each train configuration $(\sigma_1 \cdots \sigma_n)$ we show two plots: a circular one, where the magnitude of the amplitude is presented as a function of the momentum components p_x and p_y (with $p_z = 0$), and a rectangular one, where the magnitude of the probability amplitude is shown as a function of the electron kinetic energy $E_p = \mathbf{p}^2/2m_e$ and the azimuthal angle of electron detection φ_p (with $\theta_p = 0.5\pi$). In order to emphasize that the amplitude $\mathcal{A}(\mathbf{p})$ is a periodic function of φ_p , we present three copies of $|\mathcal{A}(\mathbf{p})|^\nu$ for $0 \leq \varphi_p \leq 6\pi$. It appears that, by doing so, the vortices and nodal lines will be better displayed. Results for the single pulse [Figs. 3(a) and 3(e)] clearly exhibit the multiphoton structure in the signal of ionization. Indeed, for an infinite plane wave one expects the presence of well-defined δ peaks in the probability rates, located at energies $E_N = E_B - U_p + N\omega$, where $U_p = (e\eta_E \mathcal{E}_0)^2/2m_e\omega^2$ is the ponderomotive energy associated with the circularly polarized plane wave and $\eta_E \mathcal{E}_0$ is the amplitude of the electric-field strength. In contrast, for finite pulses, these peaks manifest themselves as broad humps of finite heights in the probability distributions. For the values of E_B , η_E , and ω considered here we get $E_N = 0.78, 2.33$, and 3.88 eV for $N = 1, 2$, and 3 , respectively (plane-wave estimations). On the other hand, for $N_{\text{osc}} = 4$ and $\varphi_p = \pi$ we can roughly estimate these energies to be $0.72, 2.25$, and 3.9 eV, which agree fairly well with the predictions that follow from the plane-wave analysis. There is however an important difference: Although in the polar plots the multiphoton peaks are represented by rings, in the rectangular plots they show up as wavy stripes. The reason for that is the nonvanishing value of the time average of the vector potential $\mathbf{A}(t)$ for short pulses. Moreover, as it clearly follows from the analysis presented above, vortex structures appear in between multiphoton peaks (deep minima in the probability amplitude can be found there), where the ionization signal is marginally small. This makes the experimental detection of them practically impossible.

We see that the vortices in the distributions are present already for a single pulse in the configuration (+). For E_p not larger than 2 eV and for $N_{\text{osc}} = 4$ or 5 we observe two vortices for $\varphi_p = 0$ or π (one vortex is located very close to the origin). Such structures appear as deep-blue isolated points in the rectangular plots [see Figs. 3(a) and 3(e)]. In contrast, for the train of two pulses in the configuration (+−) we detect only nodal lines represented either by the Fermat-type spirals in the polar plots or by U-shape lines in the rectangular plots. Their tips are located at the position where the vortices appeared for the configuration (+).² Moreover, when passing from the one-photon peak to the two-photon peak we observe the ram-

ification of the nodal lines (or Fermat-type spirals) of type \mathbb{U} or \cup^U . Sometimes, such a doubling of a particular spiral might look like a trident ramification of a single nodal line [see, e.g., the case for $N_{\text{osc}} = 5$ in Fig. 3(f)], but in fact we observe a tiny avoided crossing of the nodal lines located where the vortex in the configuration (+) appeared [compare with Fig. 3(e)]. The absence of vortex structures for the configurations (+−) and (−+) is also supported by the vanishing circulation of the amplitude phase gradient. These findings are very similar to the ones presented in Ref. [45] and show that, within the approximations made in our theoretical analysis, the vortex structures exist already for single pulses of the type (+) or (−). However, for laser trains in the configurations (+−) and (−+), the vortices disappear (or are transmuted into spiral lines). This is independent of the laser pulse wavelength and the number of cycles.

As mentioned above, the vortices appear in between multiphoton peaks, where the ionization signal is very small. This could severely prevent possible experimental detection of them. Thus, important questions arise: Can one control the positions of vortices such that they appear for momenta for which the ionization signal is maximum? Can one create, by properly adjusted laser pulses, structured multiphoton peaks that exhibit both spirals and vortices?

In order to investigate these problems, one has to go beyond the configurations considered so far. Ionization (or in our case, photodetachment) driven by more complex trains of pulses needs to be analyzed. To this end, in Figs. 3(c) and 3(g) and Figs. 3(d) and 3(h) we present the results for the configurations (+ − +) and (+ + −), respectively, for which the time-dependent vector potential $\mathbf{A}(t)$ and the electric field $\mathcal{E}(t)$ are presented in Figs. 1 and 2. Independently of the fact that the time dependences of the electric fields for these configurations are very similar, the probability distributions of photoelectrons exhibit different structures, which is due to the interference of amplitudes related to the individual pulses in the corresponding sequences as well as to their time ordering. This difference can be seen clearly on the rectangular plots. For the configuration (+ − +) [Figs. 3(c) and 3(g)] and for the peak corresponding to the one-photon detachment we observe a regular honeycomb structure in the distributions for both $N_{\text{osc}} = 4$ and $N_{\text{osc}} = 5$ (we call it the vortex lattice, as it resembles similar, but not necessarily hexagonal, structures observed in superconductivity [78]). For the two-photon peak this pattern is repeated with a denser packing of hexagonal cells [this follows from the doubling of the nodal lines for the configuration (+−)]. In contrast, for the configuration (+ + −) [Figs. 3(d) and 3(h)] the spiral-type structure observed for (+−) is preserved, but additionally new vortices are created in the middle of the one-photon peak. A closer look at the rectangular plot reveals that also for this configuration we observe the honeycomb structure, but with the irregular hexagons elongated in the direction of increasing φ_p and E_p . In both configurations, the new vortices are surrounded by regions of maximum probability (or are embedded into the multiphoton peaks, where the ionization signal is maximum), which makes their experimental detection easier. Note also that the visualization of vortex structures looks better on the rectangular plots than on the polar ones. This is because, in the latter case, the vortices are stretched along

²The transmutation of the vortex for the configuration (+) into the tip of the U-shape nodal line for the configuration (+−) takes place for the particular carrier envelope phases $\chi = 0$ or π , as in these cases the positions of vortices for the configurations (+) and (−) are the same. For other phases the situation is more complicated and its investigation is beyond the scope of the present analysis.

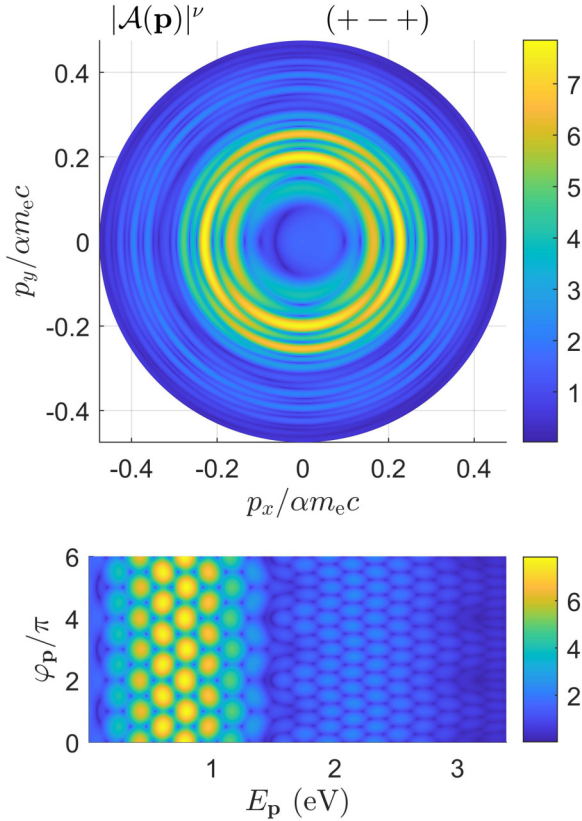


FIG. 4. SFA analysis for $N_{\text{osc}} = 4$, $\theta_p = 0.4\pi$, and the configuration $(+ - +)$. The remaining laser pulse parameters are the same as in Fig. 3. The amplitude $\mathcal{A}(\mathbf{p})$ is presented in atomic units and $\nu = 1/2$ is chosen for visual purposes.

circles, which could lead to their misinterpretation as nodal lines.

A. Robustness of vortex structures

In experimental setups the photoelectron distribution is measured with finite energy and angular resolutions. The results presented in Fig. 3 suggest that the resolutions $\Delta E_p = 0.1$ eV and $\Delta\varphi_p = 0.1\pi$ are sufficient for the experimental observation of vortex structures for laser pulses containing $N_{\text{osc}} = 4$ or 5 cycles. Still, the open question is how these patterns depend on the polar angle θ_p . To this end, we present in Fig. 4 the modulus of the amplitude $\mathcal{A}(\mathbf{p})$ for $\theta_p = 0.4\pi$, $N_{\text{osc}} = 4$, and the configuration $(+ - +)$. On the polar plot, we present it in the plane (p_x, p_y) (i.e., we show the projection of the probability amplitude calculated on the conical surface with the axis along the \mathbf{e}_z unit vector and with a half-opening angle $\theta_p = 0.4\pi$), whereas on the rectangular plot we keep the same horizontal axis as before, i.e., the kinetic energy of photoelectrons E_p . The comparison of this rectangular plot with the corresponding one in Fig. 3(c) shows a very similar structure with almost the same positions of vortices in the plane (E_p, φ_p) . In order to ensure that this is indeed the case, we calculate the circulation (or the so-called topological

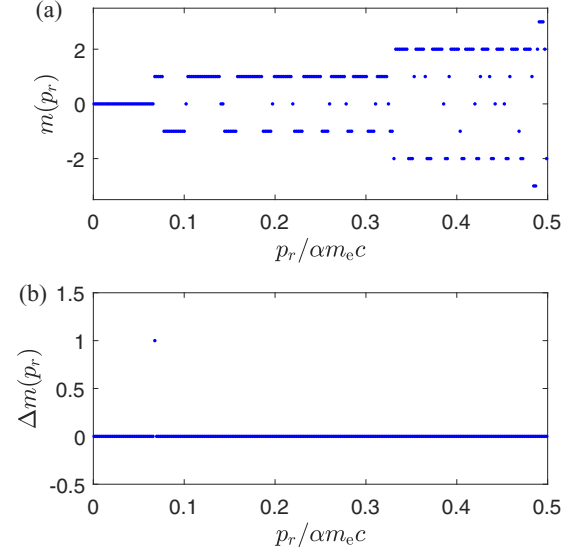


FIG. 5. (a) Topological charge $m(p_r)$ [see Eq. (37)] as a function of the photoelectron momentum $p_r = \sqrt{2m_e E_p}$ for the polar angle $\theta_p = 0.5\pi$. The laser-field parameters are $\omega = 1.5498$ eV, $\eta_{\mathcal{E}} = 0.002$, and $N_{\text{osc}} = 4$. (b) Difference of topological charges calculated at the polar angles $\theta_p = 0.5\pi$ and 0.4π [cf. Eq. (38)]. Among 250 points, only one value of p_r gives a nonvanishing difference, which indicates the robustness of the vortex locations in the rectangular plane (E_p, φ_p) .

charge) $m(p_r)$,

$$\begin{aligned} m(p_r) &= \frac{1}{2\pi} \oint_{C(p_r)} (\nabla_{\mathbf{p}} \arg[\mathcal{A}(\mathbf{p})]) \cdot d\mathbf{p} \\ &= \frac{1}{2\pi} \int_0^{2\pi} d\varphi_p \left(\frac{\partial \arg[\mathcal{A}(\mathbf{p})]}{\partial \varphi_p} \right) \Big|_{|\mathbf{p}|=p_r}, \end{aligned} \quad (37)$$

where the counterclockwise oriented circle $C(p_r)$ is defined such that $p_x^2 + p_y^2 = p_r^2 \sin^2 \theta_p$ and $p_z = p_r \cos \theta_p$. It is known that this quantity acquires integer values and in general depends on both $p_r = \sqrt{2m_e E_p}$ and θ_p . However, to simplify the notation, we neglect the dependence on the polar angle θ_p for a reason which will soon be clear.

In Fig. 5(a) we present the circulation $m(p_r)$ calculated for $\theta_p = 0.5\pi$, $N_{\text{osc}} = 4$, and the same remaining parameters as in Fig. 3. As expected, the circulation acquires integer values and jumps whenever the contour $C(p_r)$ encircles new vortices. In order to verify the robustness of this pattern against the change of the polar angle, we also calculate the circulation for $\theta_p = 0.4\pi$ and present the difference

$$\Delta m(p_r) = m(p_r)|_{\theta_p=0.5\pi} - m(p_r)|_{\theta_p=0.4\pi} \quad (38)$$

in Fig. 5(b). The calculation of $m(p_r)$ has been done either by applying the trapezoid integration scheme for the φ_p integral in (37) or by evaluating the Fourier transform, in both cases with 2^{14} points. We see that, except for a single point, this difference is equal to 0, which indicates that the positions of vortices in the (E_p, φ_p) plane are in principle independent of the polar angle θ_p , at least within the interval $[0.4\pi, 0.6\pi]$. This suggests that the collection of experimental data with

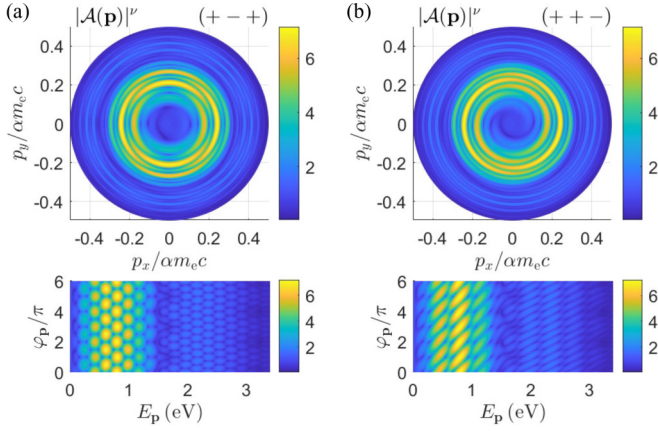


FIG. 6. TDSE analysis of photodetachment for two train configurations (a) (+ - +) and (b) (+ + -). Each single pulse comprises $N_{\text{osc}} = 4$ oscillations and the polar angle of photoelectron detection is $\theta_p = 0.5\pi$. The remaining laser pulse parameters are the same as in Fig. 3. We observe very good agreement between the TDSE and the SFA analyses, with the only difference being an overall scaling factor. The amplitudes $\mathcal{A}(\mathbf{p})$ are presented in atomic units and $\nu = 1/2$ is chosen for visual purposes.

the angular resolution $\Delta\theta_p = 0.1\pi$ should not erase the vortex structures observed for $\theta_p = 0.5\pi$.

Note that $\Delta m(p_r)$ vanishes nearly for all points also for much larger laser intensities corresponding, for instance, to $\eta_{\mathcal{E}} = 0.01$. However, for such intensities the applicability of the SFA in the low-energy part of the spectra of photoelectrons might be questionable due to significant depletion effects between the pulses and due to rescattering processes.

B. TDSE analysis

The SFA, which is the approach considered so far, has limited validity. First, because of the Born approximation applied to the final scattering state of photoelectrons, this approach can be appropriate for the high-energy part of the photoelectron spectrum. Second, as discussed in [45,66], it can be used for the low-energy part of the spectrum provided the total ionization probability is smaller than 1; hence, the intensity of the laser pulse cannot be arbitrarily large. Under such circumstances, the depletion and rescattering effects are small (in fact, these effects could spoil or significantly modify the subtle vortex and spiral structures of multiphoton peaks discussed here) and we can expect to reach good agreement with the TDSE analysis. This has been demonstrated in our previous study [45] of low-frequency laser pulses. There we showed very good agreement between the SFA and TDSE approaches for the configuration (+ -). For this particular train of configuration, only spiral structures were observed in the probability amplitude of detachment and no vortices were detected. In order to go beyond our previous studies and to observe both the spirals and vortex structures embedded into multiphoton peaks, we have considered above the configurations (+ + -) and (+ - +). In Fig. 6 we present the TDSE analysis of photodetachment for the short-range (Yukawa) potential model [see Eq. (31)]. The driving field consists of trains of laser pulses in the configurations (+ - +) and (+ + -);

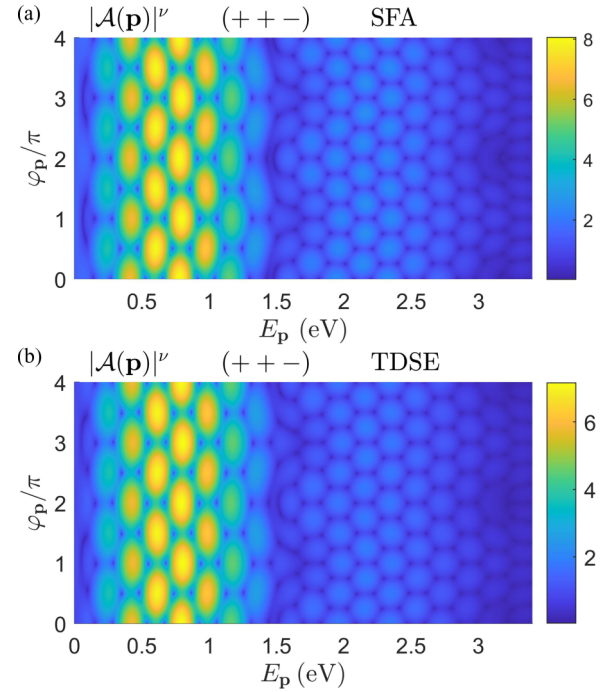


FIG. 7. Comparison of the (a) SFA and (b) TDSE analyses of photodetachment for the configuration (+ + -) and $N_{\text{osc}} = 4$. The remaining laser-field parameters are the same as in Fig. 3. We see that the positions of vortices are independent of the theoretical approach being applied. The main difference between the two figures is an overall scaling factor, which can be easily introduced in the parameter A of Eq. (27). The amplitudes $\mathcal{A}(\mathbf{p})$ are presented in atomic units and $\nu = 1/2$ is chosen for visual purposes.

each one comprises $N_{\text{osc}} = 4$ laser cycles. The remaining laser-field parameters are the same as in Fig. 3. Comparison of the rectangular plots in Fig. 6 with the corresponding ones in Fig. 3 [i.e., Figs. 3(c) and 3(d)] shows astonishing agreement of the photodetachment patterns obtained from the SFA and TDSE with in principle the same positions of vortices embedded into multiphoton peaks. [In Fig. 7 we compare the SFA and TDSE analyses for the configuration (+ + -) in more detail.] The only difference is that TDSE predicts smaller ionization probabilities compared to the results from the SFA, but this difference can be compensated by properly adjusting the normalization factor A present in the definition of the bound state (27). This factor is in fact a fitting parameter. Thus, our investigations show the robustness of the vortex and spiral structures in multiphoton spectra against different theoretical models, hence providing a strong argument that similar structures should in principle be observed experimentally.

VI. REDUCIBLE CONFIGURATION OF PULSES

Up to now, we have considered only the irreducible configuration of pulses. Thus, the questions arise of how the photodetachment pattern discussed above is modified if the sequence of pulses is repeated a few times or if one can expect the creation of new vortices for such a reducible configuration of pulses. Providing a general answer to these questions is

difficult even if one applies purely analytical methods. The reason for that is that the photodetachment (or, in general, ionization) pattern is modified by the rescattering processes [15]. However, the common understanding of strong-field ionization is such that the rescattering modifies significantly only the high-energy portion of the spectrum. In contrast, its low-energy portion is sufficiently well described by the direct process, that is, by the SFA presented above. This conclusion is also supported by our previous investigations [44,45]. For these reasons we apply the SFA to study the problems stated above.

To this end, let us consider a general reducible configuration of pulses of the form (9) and let us assume that the irreducible configuration ($\sigma_1\sigma_2\cdots\sigma_k$) lasts for time T_1 . Hence, the entire train of pulses lasts for time ℓT_1 . The ionization amplitude for such a train can be put in the form [cf. Eq. (25)]

$$\mathcal{A}_\ell(\mathbf{p}) = \int_0^{\ell T_1} H_p(t) e^{i\tilde{G}_p(t)} e^{i(G_p)t} dt, \quad (39)$$

where

$$H_p(t) = ie\mathcal{E}(t) \cdot \tilde{\Phi}_0(\mathbf{p} - e\mathbf{A}(t)). \quad (40)$$

Moreover, by introducing the time average of an arbitrary periodic function $\mathcal{F}(t)$ with period T_1 ,

$$\langle \mathcal{F} \rangle = \frac{1}{T_1} \int_0^{T_1} \mathcal{F}(t) dt = \frac{1}{\ell T_1} \int_0^{\ell T_1} \mathcal{F}(t) dt, \quad (41)$$

we have

$$\tilde{G}_p(t) = \int_0^t \left(\frac{1}{2m_e} [\mathbf{p} - e\mathbf{A}(\tau)]^2 - E_B - \langle G_p \rangle \right) d\tau \quad (42)$$

and

$$\langle G_p \rangle = \frac{1}{2m_e} [\mathbf{p} - e\langle \mathbf{A} \rangle]^2 + \frac{e^2}{2m_e} [\langle \mathbf{A}^2 \rangle - \langle \mathbf{A} \rangle^2] - E_B. \quad (43)$$

For very long pulses the so-called displacement $\langle \mathbf{A} \rangle$ is nearly 0, but for short pulses it could acquire a significant value such that its experimental detection becomes feasible (see, e.g., [79]).

The essence of the decomposition (39) is that the functions $H_p(t)$ and $\tilde{G}_p(t)$ are periodic in time, i.e.,

$$H_p(t) = H_p(t + MT_1), \quad \tilde{G}_p(t) = \tilde{G}_p(t + MT_1) \quad (44)$$

for $M = 1, \dots, \ell - 1$ and $t \in [0, T_1]$. Due to these properties we get

$$\begin{aligned} \mathcal{A}_\ell(\mathbf{p}) &= \sum_{M=1}^{\ell} \int_{(M-1)T_1}^{MT_1} H_p(t) e^{i\tilde{G}_p(t)} e^{i(G_p)t} dt \\ &= \sum_{M=1}^{\ell} e^{i(M-1)\langle G_p \rangle T_1} \int_0^{T_1} H_p(t) e^{i\tilde{G}_p(t)} e^{i(G_p)t} dt, \end{aligned} \quad (45)$$

and after summing up the geometrical series we arrive at

$$\mathcal{A}_\ell(\mathbf{p}) = \exp\left(i\frac{\ell-1}{2}\langle G_p \rangle T_1\right) \frac{\sin(\frac{\ell}{2}\langle G_p \rangle T_1)}{\sin(\frac{1}{2}\langle G_p \rangle T_1)} \mathcal{A}_1(\mathbf{p}). \quad (46)$$

Hence, the ionization amplitude for a reducible configuration of pulses can be presented as the product of three terms.

The first one is the overall phase factor that is always different from 0 and disappears when calculating the probability distributions. The second factor with the sine functions is the typical interference term known, for instance, from the Fraunhofer diffraction [80]. The last one is the amplitude for the irreducible configuration. Thus, the reducibility of the pulse configuration introduces new nodes that follow only from the sine function in the numerator of (46). These nodes appear for momenta \mathbf{p}_L such that $\ell\langle G_{\mathbf{p}_L} \rangle T_1 = 2\pi L$ for an integer L , provided L is not a multiple of ℓ , as

$$\mathcal{A}_\ell(\mathbf{p}_L) = \begin{cases} \ell \mathcal{A}_1(\mathbf{p}_L) & \text{for } L = \ell N \\ 0 & \text{otherwise.} \end{cases} \quad (47)$$

Note that for $L = \ell N$, $N = 1, 2, \dots$, we observe a coherent enhancement of the probability amplitude, i.e., the amplitude grows linearly with ℓ . Hence, the repetition of the same laser pulse produces coherent comb structures in the probability distributions, which are present also in other quantum processes, such as Compton scattering [81], Breit-Wheeler particle-antiparticle pair creation [82], and the dynamical Sauter-Schwinger process [83].

As follows from (43), the momenta \mathbf{p}_L for these new zeros satisfy the equation

$$(\mathbf{p}_L - e\langle \mathbf{A} \rangle)^2 = P_L^2, \quad (48)$$

with

$$P_L^2 = 4\pi m_e \frac{L}{\ell T_1} - e^2(\langle \mathbf{A}^2 \rangle - \langle \mathbf{A} \rangle^2) + 2m_e E_B > 0 \quad (49)$$

for sufficiently large L . Hence, these new nodes form spheres in momentum space of radius P_L , centered at $e\langle \mathbf{A} \rangle$, and the amplitude phase $\arg[\mathcal{A}_\ell(\mathbf{p})]$, when traversing this surface, jumps by π .³ This leads us to the conclusion that the vortex structures can be created *only* by the irreducible pulse configuration and that the repetition of them only generates extra nodal surfaces in the form of concentric spheres.

Note that the neighboring spheres are distanced from each other in momentum space by

$$P_{L+1} - P_L = \frac{4\pi m_e}{\ell T_1(P_{L+1} + P_L)} \quad (50)$$

or in the energy space by

$$\frac{1}{2m_e}(P_{L+1}^2 - P_L^2) = \frac{2\pi}{\ell T_1}. \quad (51)$$

Hence, they are well separated from each other for small ℓ and T_1 , which means that the most favorable situation for the experimental verification of this analysis would be to consider the repetition of two pulses with a vanishing time delay between them. This situation is illustrated in Fig. 8 for the reducible configuration $(++) = (+)^2$ and $N_{\text{osc}} = 4$. As expected from (51), for $N_{\text{osc}} = 5$ (i.e., for larger T_1) the pattern remains qualitatively the same, but with a denser distribution

³This is the generic situation. It might happen, however, that for particular momenta the nodal surfaces or the vortex lines created by $\mathcal{A}_1(\mathbf{p})$ intersect these spheres and the phase pattern becomes more complicated.

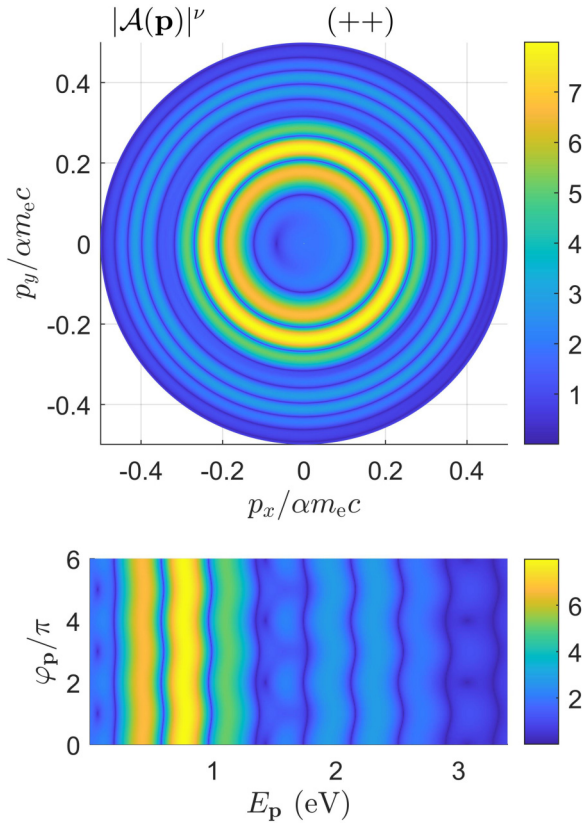


FIG. 8. SFA analysis for $N_{\text{osc}} = 4$ and the reducible configuration $(++)$. The remaining laser pulse parameters are the same as in Fig. 3. The individual one- and two-photon rings, observed in Fig. 3(a), now are split into finer structures due to the presence of extra nodal surfaces. As expected from our analysis, the repetition of the pulse does not produce new vortices. The amplitude $A(\mathbf{p})$ is presented in atomic units and $\nu = 1/2$ is chosen for visual purposes.

of nodal rings (not shown). Moreover, the time delays D_ℓ enlarge T_1 and, in consequence, also lead to denser distributions of the nodal spheres. Similar effects have been predicted for Compton and Thomson scattering [81] and for the strong-field Breit-Wheeler pair production [82,84].

VII. CONCLUSION

The theoretical investigations initiated in [34] and their subsequent experimental verification presented in [48] on the spiral structures in ionization by a sequence of two circularly polarized pulses opened a new direction in multiphoton physics. It was argued that the momentum distribution of photoelectrons corresponding to a particular multiphoton peak acquires new structures, presumably in the form of quantum vortices, as spirals are commonly attributed to vortices. Our recent analysis of photodetachment has shown that this is not *necessarily* the case. It has been demonstrated theoretically that vortex-type distributions can be generated already by

single linearly [44] or circularly [45] polarized pulses without spiral-type signatures and, in contrast, for the train of two circularly polarized pulses in the configuration $(+-)$ and for the field parameters considered, the spiral structures are created without vorticity. The fact that the spirals have been experimentally detected is because they are embedded into the multiphoton peaks. On the other hand, vortices generated by the configuration $(+)$ or $(-)$ are located at positions in the momentum space for which the ionization signal is very small. Hence, for such configurations, their experimental detection seems impossible.

The aim of this paper was to propose another experimental setup for which one can expect to detect both vortices and spirals embedded into multiphoton peaks so that their experimental verification could be easier. Such a setup would consist of a train of pulses in the configurations $(+ + -)$ and $(+ - +)$, for which we have analyzed the properties of structured multiphoton peaks for photodetachment. We have shown the robustness of these structures against small changes of photoelectron kinetic energy and emission angles, which shows that their experimental detection is feasible. Our analysis has been carried out by applying two theoretical approaches commonly used in this type of investigation. First, we applied the SFA analysis with the zero-range binding potential, which appears to be a very good theoretical tool for photodetachment of negative ions (see, e.g., the thorough theoretical studies presented in [70]). Second, we performed the TDSE analysis for the short-range Yukawa potential. For the train of laser pulses in the configurations $(+ + -)$ and $(+ - +)$ we demonstrated that both theoretical approaches used in our studies lead to the same vortex and spiral structures embedded in the multiphoton peaks. This finding could indicate that these structures are determined solely by the properties of the laser pulse, provided its intensity is not too large to neglect the depletion and rescattering effects.

The fact that the vortex and spiral structures discussed in this paper are to some extent independent of the theoretical models for atomic systems (i.e., of the form of the Hamiltonian without the electron–laser-field interaction term) allows us to expect that similar patterns can be observed also for systems with the Coulomb tail. It is known that in quantum mechanics, such systems need special attention and it is an open question whether the SFA with appropriate Coulomb corrections can provide equally good agreement with the TDSE analysis.

ACKNOWLEDGMENTS

This work was supported by the National Natural Science Foundation of China through Grants No. 11961131008 and No. 11725416, by the National Key R&D Program of China through Grant No. 2018YFA0306302 (L.G. and L.-Y.P.), and by the National Science Centre (Poland) under Grants No. 2018/31/B/ST2/01251 (F.C.V.) and No. 2018/30/Q/ST2/00236 (J.Z.K. and K.K.).

L.G. and F.C.V. contributed equally to this work.

[1] P. Agostini, F. Fabre, G. Mainfray, G. Petite, and N. K. Rahman, *Phys. Rev. Lett.* **42**, 1127 (1979).

[2] P. Kruij, J. Kimman, and M. J. van der Wiel, *J. Phys. B* **14**, L597 (1981).

- [3] P. Kruit, J. Kimman, H. G. Muller, and M. J. van der Wiel, *Phys. Rev. A* **28**, 248 (1983).
- [4] A. McPherson, G. Gibson, H. Jara, U. Johann, T. S. Luk, I. A. McIntyre, K. Boyer, and C. K. Rhodes, *J. Opt. Soc. Am. B* **4**, 595 (1987).
- [5] M. Ferray, A. L'Huillier, X. F. Li, L. A. Lompre, G. Mainfray, and C. Manus, *J. Phys. B* **21**, L31 (1988).
- [6] G. Farkas and C. Tóth, *Phys. Lett. A* **168**, 447 (1992).
- [7] T. Brabec and F. Krausz, *Rev. Mod. Phys.* **72**, 545 (2000).
- [8] F. Krausz and M. Ivanov, *Rev. Mod. Phys.* **81**, 163 (2009).
- [9] D. Strickland and G. Mourou, *Opt. Commun.* **56**, 219 (1985).
- [10] M. Protopapas, C. H. Keitel, and P. L. Knight, *Rep. Prog. Phys.* **60**, 389 (1997).
- [11] F. Ehlotzky, A. Jaroń, and J. Z. Kamiński, *Phys. Rep.* **297**, 63 (1998).
- [12] F. Ehlotzky, *Phys. Rep.* **345**, 175 (2001).
- [13] P. Agostini and L. F. DiMauro, *Rep. Prog. Phys.* **67**, 813 (2004).
- [14] A. Becker and F. H. M. Faisal, *J. Phys. B* **38**, R1 (2005).
- [15] D. B. Milošević, G. G. Paulus, D. Bauer, and W. Becker, *J. Phys. B* **39**, R203 (2006).
- [16] C. J. Joachain, N. J. Kylstra, and R. M. Potvliege, *Atoms in Intense Laser Fields* (Cambridge University Press, Cambridge, 2011).
- [17] L.-Y. Peng, W.-C. Jiang, J.-W. Geng, W.-H. Xiong, and Q. Gong, *Phys. Rep.* **575**, 1 (2015).
- [18] C. F. de Morisson Faria and A. S. Maxwell, *Rep. Prog. Phys.* **83**, 034401 (2020).
- [19] S. P. Roshchupkin, *Laser Phys.* **6**, 837 (1996).
- [20] G. A. Mourou, T. Tajima, and S. V. Bulanov, *Rev. Mod. Phys.* **78**, 309 (2006).
- [21] Y. I. Salamin, S. X. Hu, K. Z. Hatsagortsyan, and C. H. Keitel, *Phys. Rep.* **427**, 41 (2006).
- [22] F. Ehlotzky, K. Krajewska, and J. Z. Kamiński, *Rep. Prog. Phys.* **72**, 046401 (2009).
- [23] A. Di Piazza, C. Müller, K. Z. Hatsagortsyan, and C. H. Keitel, *Rev. Mod. Phys.* **84**, 1177 (2012).
- [24] F. Cajiao Vélez, J. Z. Kamiński, and K. Krajewska, *Atoms* **7**, 34 (2019).
- [25] H. Hu, *Contemp. Phys.* **61**, 12 (2020).
- [26] P. Zhang, S. S. Bulanov, D. Seipt, A. V. Arefiev, and A. G. R. Thomas, *Phys. Plasmas* **27**, 050601 (2020).
- [27] U. I. Uggerhøj, *Rev. Mod. Phys.* **77**, 1131 (2005).
- [28] E. Esarey, C. B. Schroeder, and W. P. Leemans, *Rev. Mod. Phys.* **81**, 1229 (2009).
- [29] L. V. Keldysh, *Zh. Eksp. Teor. Fiz.* **47**, 1945 (1964) [*Sov. Phys. JETP* **20**, 1307 (1965)].
- [30] S. V. Popruzhenko, *J. Phys. B* **47**, 204001 (2014).
- [31] K. Amini, J. Biegert, F. Calegari *et al.*, *Rep. Prog. Phys.* **82**, 116001 (2019).
- [32] F. H. M. Faisal, *J. Phys. B* **6**, L89 (1973).
- [33] H. R. Reiss, *Phys. Rev. A* **22**, 1786 (1980).
- [34] J. M. N. Djiokap, S. X. Hu, L. B. Madsen, N. L. Manakov, A. V. Meremianin, and A. F. Starace, *Phys. Rev. Lett.* **115**, 113004 (2015).
- [35] J. M. N. Djiokap, A. V. Meremianin, N. L. Manakov, S. X. Hu, L. B. Madsen, and A. F. Starace, *Phys. Rev. A* **94**, 013408 (2016).
- [36] J. M. N. Djiokap, A. V. Meremianin, N. L. Manakov, S. X. Hu, L. B. Madsen, and A. F. Starace, *Phys. Rev. A* **96**, 013405 (2017).
- [37] K. J. Yuan, S. Chelkowski, and A. D. Bandrauk, *Phys. Rev. A* **93**, 053425 (2016).
- [38] K. J. Yuan, H. Lu, and A. D. Bandrauk, *J. Phys. B* **50**, 124004 (2017).
- [39] M. Li, G. Zhang, X. Kong, T. Wang, X. Ding, and J. Yao, *Opt. Express* **26**, 878 (2018).
- [40] N. V. Larionov, S. Y. Ovchinnikov, A. A. Smirnovsky, and A. A. Schmidt, *Tech. Phys.* **63**, 1569 (2018).
- [41] N. V. Larionov, D. N. Makarov, A. A. Smirnovsky, and S. Y. Ovchinnikov, *Zh. Eksp. Teor. Fiz.* **156**, 1035 (2019) [*J. Exp. Theor. Phys.* **129**, 949 (2019)].
- [42] T. Bayer, C. Philipp, K. Eickhoff, and M. Wollenhaupt, *Phys. Rev. A* **102**, 013104 (2020).
- [43] A. S. Maxwell, C. Figueira de Morisson Faria, X. Y. Lai, R. P. Sun, and X. J. Liu, *Phys. Rev. A* **102**, 033111 (2020).
- [44] F. Cajiao Vélez, L. Geng, J. Z. Kamiński, L.-Y. Peng, and K. Krajewska, *Phys. Rev. A* **102**, 043102 (2020).
- [45] L. Geng, F. Cajiao Vélez, J. Z. Kamiński, L.-Y. Peng, and K. Krajewska, *Phys. Rev. A* **102**, 043117 (2020).
- [46] A. S. Maxwell, G. S. J. Armstrong, M. Ciappina, E. Pisanty, Y. Kang, A. Brown, M. Lewenstein, and C. Figueira de Morisson Faria, *Faraday Discuss.* **228**, 394 (2021).
- [47] Y. Kang, E. Pisanty, M. Ciappina, M. Lewenstein, C. Figueira de Morisson Faria, and A. S. Maxwell, *Eur. Phys. J. D* **75**, 199 (2021).
- [48] D. Pengel, S. Kerbstadt, D. Johannmeyer, L. Englert, T. Bayer, and M. Wollenhaupt, *Phys. Rev. Lett.* **118**, 053003 (2017).
- [49] S. Kerbstadt, K. Eickhoff, T. Bayer, and M. Wollenhaupt, *Nat. Commun.* **10**, 658 (2019).
- [50] S. Kerbstadt, K. Eickhoff, T. Bayer, and M. Wollenhaupt, *Adv. Phys. X* **4**, 1672583 (2019).
- [51] K. Eickhoff, D. Köhnke, L. Feld, L. Englert, T. Bayer, and M. Wollenhaupt, *New J. Phys.* **22**, 123015 (2020).
- [52] K. Eickhoff, C. Rathje, D. Köhnke, S. Kerbstadt, L. Englert, T. Bayer, S. Schäfer, and M. Wollenhaupt, *New J. Phys.* **22**, 103045 (2020).
- [53] *Spirals and Vortices in Culture, Nature, and Science*, edited by K. Tsuji and S. C. Müller (Springer, Cham, 2019).
- [54] H. von Helmholtz, *Philos. Mag.* **33**, 485 (1867).
- [55] W. Thomson, *Philos. Mag.* **34**, 15 (1867).
- [56] P. A. M. Dirac, *Proc. R. Soc. London Ser. A* **133**, 60 (1931).
- [57] W. F. Viven, *Proc. R. Soc. London Ser. A* **260**, 218 (1961).
- [58] S. M. Lloyd, M. Babiker, G. Thirunavukkarasu, and J. Yuan, *Rev. Mod. Phys.* **89**, 035004 (2017).
- [59] K. Y. Bliokh, I. P. Ivanov, G. Guzzinati, L. Clark, R. Van Boxem, A. Béché, R. Juchtmans, M. A. Alonso, P. Schattschneider, F. Nori, and J. Verbeeck, *Phys. Rep.* **690**, 1 (2017).
- [60] K. Krajewska and J. Z. Kamiński, *Phys. Rev. B* **68**, 064418 (2003).
- [61] K. Krajewska, J. Z. Kamiński, and R. M. Potvliege, *Ann. Phys. (NY)* **323**, 2639 (2008).
- [62] J. H. Macek, J. B. Sternberg, S. Y. Ovchinnikov, T.-G. Lee, and D. R. Schultz, *Phys. Rev. Lett.* **102**, 143201 (2009).
- [63] J. H. Macek, J. B. Sternberg, S. Y. Ovchinnikov, and J. S. Briggs, *Phys. Rev. Lett.* **104**, 033201 (2010).
- [64] C. M. DeMars, S. J. Ward, J. Colgan, S. Amami, and D. H. Madison, *Atoms* **8**, 26 (2020).
- [65] F. Cajiao Vélez, K. Krajewska, and J. Z. Kamiński, *Phys. Rev. A* **97**, 043421 (2018).

- [66] F. Cajiao Vélez, J. Z. Kamiński, and K. Krajewska, *Phys. Rev. A* **101**, 053430 (2020).
- [67] I. Białynicki-Birula, M. Cieplak, and J. Kamiński, *Theory of Quanta* (Oxford University Press, New York, 1992).
- [68] I. Białynicki-Birula, Z. Białynicki-Birula, and C. Śliwa, *Phys. Rev. A* **61**, 032110 (2000).
- [69] A. J. Taylor, *Analysis of Quantised Vortex Tangle* (Springer, Cham, 2017).
- [70] G. F. Gribakin and M. Y. Kuchiev, *Phys. Rev. A* **55**, 3760 (1997).
- [71] L. Rodberg and R. Thaler, *Introduction to the Quantum Theory of Scattering* (Academic, New York, 1967).
- [72] J. R. Taylor, *Scattering Theory: The Quantum Theory of Non-relativistic Collisions* (Wiley, New York, 1972).
- [73] M. Crance, *J. Phys. B* **20**, L411 (1987).
- [74] M. Crance, *J. Phys. B* **20**, 6553 (1987).
- [75] M. Crance, *J. Phys. B* **21**, 3559 (1988).
- [76] B. M. Smirnov, *Physics of Atoms and Ions* (Springer, New York, 2003).
- [77] D. M. Wolkow, *Z. Phys.* **94**, 250 (1935). Very interesting generalizations of the Volkov states can be found in: M. Gavrilá, *Phys. Rev. A* **99**, 012120 (2019); A. Di Piazza, *Phys. Rev. D* **103**, 076011 (2021).
- [78] A. A. Abrikosov, *Fundamentals of the Theory of Metals* (Elsevier Science, Oxford, 1988).
- [79] X.-R. Xiao, M.-X. Wang, H. Liang, Q. Gong, and L.-Y. Peng, *Phys. Rev. Lett.* **122**, 053201 (2019).
- [80] M. Born and E. Wolf, *Principles of Optics* (Cambridge University Press, Cambridge, 1999).
- [81] K. Krajewska, M. Twardy, and J. Z. Kamiński, *Phys. Rev. A* **89**, 052123 (2014).
- [82] K. Krajewska and J. Z. Kamiński, *Phys. Rev. A* **90**, 052108 (2014).
- [83] J. Z. Kamiński, M. Twardy, and K. Krajewska, *Phys. Rev. D* **98**, 056009 (2018); K. Krajewska and J. Z. Kamiński, *Phys. Rev. A* **100**, 062116 (2019).
- [84] M. J. A. Jansen and C. Müller, *Phys. Lett. B* **766**, 71 (2017).